Guided resonance fluorescence of a single emitter after pulsed excitation

Kazuki Koshino[1] and Takao Aoki[2]
[1]*College of Liberal Arts and Sciences, Tokyo Medical and Dental University, Ichikawa, Chiba 272-0827, Japan*
[2]*Department of Applied Physics, Waseda University, Shinjuku, Tokyo 169-8555, Japan*
(Received 14 October 2013; published 11 February 2014)

We theoretically investigated a microtoroidal cavity quantum electrodynamics system in which radiation from the emitter is nearly perfectly guided into a fiber mode, and analyzed the resonance fluorescence from the emitter after pulsed excitation. We derived analytic formulas to rigorously evaluate the photon statistics of the pulse emitted into the fiber, and clarified the conditions needed for the excitation pulse to generate single- and two-photon pulses.

DOI: 10.1103/PhysRevA.89.023814 PACS number(s): 42.50.Ar, 42.50.Pq, 42.65.Sf

I. INTRODUCTION

Photons can retain quantum coherence for a long time, making them promising carriers of quantum information. Therefore, technologies for the generation, manipulation, and detection of single photons are being rapidly developed in modern photonics. In particular, since the use of optical fibers is practically inevitable, on-demand generation of indistinguishable single photons directly into an optical fiber is highly desired.

A natural idea for such a single-photon source is to use the spontaneous emission of quantum emitters. The representative candidates of single-photon emitters are atoms [1–6], ions [7,8], and their solid-state counterparts such as color centers in diamond [9–12] and semiconductor quantum dots [13–15]. It has been confirmed that the fluorescence from these emitters exhibits sub-Poissonian photon statistics, i.e., $g^{(2)}(0) < 1$. Extensive efforts are being made to efficiently guide the spontaneous emission from these emitters into a target fiber. The collection efficiency is often quantified by the β factor, which is the emission rate into the target mode normalized by the total decay rate. It was recently found that a considerable fraction of the emission can be guided into the target mode simply by placing the emitters close to a tapered fiber, but the collection efficiency was still far below unity [16–24]. To achieve a collection efficiency close to unity, the use of an optical cavity and the resultant Purcell effect seems promising. Particularly, fiber-coupled cavity quantum electrodynamics (QED) systems with microtoroidal cavities [25–28] exhibit both a high β factor and coupling efficiency to single-mode optical fibers.

In this article, we theoretically investigated a practical cavity QED setup, the schematic of which is illustrated in Fig. 1: A quantum dot is coupled to a microtoroidal cavity, which is further coupled to a tapered fiber. The dot is driven by an excitation pulse applied from the side. The two ends of the fiber are mixed by a beam splitter to form a Sagnac interferometer, which is adjusted so that the emission from the dot is forwarded to one end of the fiber. We derived analytic formulas to determine the photon statistics of a generated pulse, and numerically evaluated the photon statistics with realistic cavity QED parameters. It is shown that nearly ideal single-photon pulses with a one-photon probability of 0.97 and a multiphoton probability of 0.01 can be generated by optimizing the excitation pulse.

The rest of this paper is organized as follows. The theoretical model is presented in Sec. II and the analytical formulas used to determine the output photon statistics are derived in Sec. III. Assuming realistic cavity QED parameters, the photon statistics are numerically evaluated in Sec. IV. A summary is given in Section V.

II. SYSTEM

The schematic of the setup is shown in Fig. 1. It is composed of a quantum dot driven by an excitation pulse, a microtoroidal cavity, and a tapered fiber forming a Sagnac interferometer. Setting $\hbar = c = 1$, the Hamiltonian of the overall system is

$$\mathcal{H} = \mathcal{H}_1 + \mathcal{H}_2 + \mathcal{H}_3 + \mathcal{H}_4, \tag{1}$$

$$\mathcal{H}_1 = \omega_d \sigma^\dagger \sigma + \omega_c (a^\dagger a + b^\dagger b) + g[\sigma^\dagger (a + b) + (a^\dagger + b^\dagger)\sigma], \tag{2}$$

$$\mathcal{H}_2 = if(t)\sigma^\dagger - if^*(t)\sigma, \tag{3}$$

$$\mathcal{H}_3 = \int dk[k a_k^\dagger a_k + \sqrt{\kappa/2\pi}(a^\dagger a_k + a_k^\dagger a)] + \int dk[k b_k^\dagger b_k + \sqrt{\kappa/2\pi}(b^\dagger b_k + b_k^\dagger b)], \tag{4}$$

$$\mathcal{H}_4 = \int dk[k c_k^\dagger c_k + \sqrt{\gamma/2\pi}(\sigma^\dagger c_k + c_k^\dagger \sigma)], \tag{5}$$

where $\mathcal{H}_1$ describes the coherent interaction between the dot and the cavity vacuum modes, $\mathcal{H}_2$ describes the driving of the dot by the excitation pulse, $\mathcal{H}_3$ describes the cavity leakage into the fiber, and $\mathcal{H}_4$ describes the radiative decay of the dot into free space. Note that the toroidal cavity supports two degenerate counter-rotating modes. The parameters are defined as follows. ω_d and ω_c respectively are the resonance frequencies of the dot and the two cavity modes, g is the coherent coupling between them, κ is the leak rate of the cavity modes into the fiber, and γ is the radiative decay rate of the dot into free space. The meanings of the operators are as follows. σ, a, and b respectively denote the annihilation operators for the dot excitation and the two counter-rotating modes of the toroidal cavity. a_k and b_k respectively denote the field operators

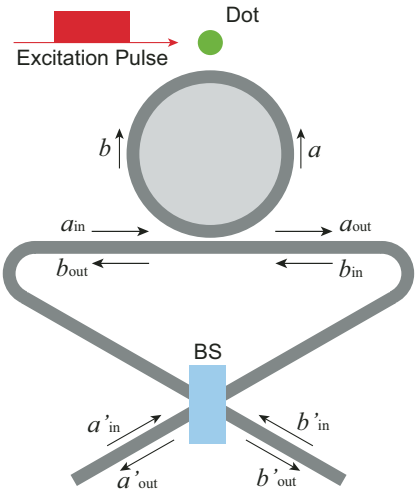

FIG. 1. (Color online) Schematic of the toroidal cavity QED system considered. A quantum dot is coupled to a toroidal cavity and then to a fiber. The dot is driven by an excitation pulse applied from the side. The emitted photon is always forwarded to one of the two fiber ends.

for two counter-propagating modes of the fiber with wave number k, and c_k denotes the field operator for a free-space photon (Fig. 1). The real-space representation of a_k is defined by the Fourier transform as $\widetilde{a}_r = (2\pi)^{-1/2}\int dk e^{ikr}a_k$. In this representation, the propagating fields interact with the cavity at $r = 0$. The input and output field operators are defined by $a_{\rm in}(t) = \widetilde{a}_{-0}(t)$ and $a_{\rm out}(t) = \widetilde{a}_{+0}(t)$, respectively. $b_{\rm in}(t)$ and $b_{\rm out}(t)$ are defined similarly.

Throughout this study, we focus on the case of $\omega_d = \omega_c$. Initially, the dot-cavity system is in its ground state. Its state vector is given by

$$|\psi_i\rangle = |0\rangle. \tag{6}$$

The dot is excited at $t = 0$ by a resonant square pulse with pulse length T and amplitude $\Omega/2$, where Ω is the Rabi frequency. The excitation pulse is then given by

$$f(t) = (\Omega/2)e^{-i\omega_d t}\theta(t)\theta(T-t), \tag{7}$$

where $\theta(t)$ is the Heaviside step function.

Three comments are in order regarding this model. (i) A typical frequency separation between two adjacent modes of a microtoroidal resonator is larger than 10 GHz, which is sufficiently larger than the cavity-enhanced decay rate of the dot considered here ($\Gamma = 4g^2/\kappa = 2\pi \times 160$ MHz; see Sec. IV). Therefore, the coupling to other cavity modes is negligible. (ii) The coupling between the left-right modes due to the surface roughness of the microtoroidal resonator breaks the left-right symmetry of the model. However, a typical left-right coupling is a few MHz, which is sufficiently smaller than the cavity linewidth ($\kappa = 2\pi \times 1000$ MHz; see Sec. IV). Therefore, the broken left-right symmetry is also negligible. (iii) We neglected the losses in the optical fiber and the beam splitter, assuming typical experimental setups.

III. ANALYSIS

A. Heisenberg equations

Our analysis is based on the Heisenberg equations that are derivable from the Hamiltonian of Eq. (1). Switching to a frame rotating at ω_d ($=\omega_c$), the Heisenberg equations for the dot and cavity operators are given by

$$\frac{d}{dt}\sigma = -\frac{\gamma}{2}\sigma - f(t)[\sigma^\dagger,\sigma] + ig[\sigma^\dagger,\sigma](a+b) + i\sqrt{\gamma}[\sigma^\dagger,\sigma]c_{\rm in}(t), \tag{8}$$

$$\frac{d}{dt}a = -\frac{\kappa}{2}a - ig\sigma - i\sqrt{\kappa}a_{\rm in}(t), \tag{9}$$

$$\frac{d}{dt}b = -\frac{\kappa}{2}b - ig\sigma - i\sqrt{\kappa}b_{\rm in}(t), \tag{10}$$

and the input-output relations for the propagating fields are given by

$$a_{\rm out}(t) = a_{\rm in}(t) - i\sqrt{\kappa}a(t), \tag{11}$$

$$b_{\rm out}(t) = b_{\rm in}(t) - i\sqrt{\kappa}b(t). \tag{12}$$

We assume that our setup is in the weak-coupling regime ($\kappa > g$), which is known to be advantageous for efficient guiding of the radiation from the dot to the fiber [27]. In this regime, we can eliminate the cavity operators adiabatically. Then we have

$$\frac{d}{dt}\sigma = -\frac{\Gamma_t}{2}\sigma - f(t)[\sigma^\dagger,\sigma] + \sqrt{\Gamma}[\sigma^\dagger,\sigma][a_{\rm in}(t)+b_{\rm in}(t)] + i\sqrt{\gamma}[\sigma^\dagger,\sigma]c_{\rm in}(t), \tag{13}$$

$$a_{\rm out}(t) = -a_{\rm in}(t) - \sqrt{\Gamma}\sigma(t), \tag{14}$$

$$b_{\rm out}(t) = -b_{\rm in}(t) - \sqrt{\Gamma}\sigma(t), \tag{15}$$

where $\Gamma = 4g^2/\kappa$ is the decay rate of the dot into the fiber and $\Gamma_t = 2\Gamma + \gamma$ is the overall decay rate of the dot.

In the present setup, the input and output ports of the fiber are mixed by a beam splitter. Defining $a'_{\rm in}$, $b'_{\rm in}$, $a'_{\rm out}$, and $b'_{\rm out}$ as shown in Fig. 1, the beam splitter functions as

$$\begin{pmatrix} a_{\rm in} \\ b_{\rm in} \end{pmatrix} = \frac{1}{\sqrt{2}}\begin{pmatrix} ie^{i\theta} & 1 \\ 1 & ie^{-i\theta} \end{pmatrix}\begin{pmatrix} a'_{\rm in} \\ b'_{\rm in} \end{pmatrix}, \tag{16}$$

$$\begin{pmatrix} a'_{\rm out} \\ b'_{\rm out} \end{pmatrix} = \frac{1}{\sqrt{2}}\begin{pmatrix} 1 & ie^{i\theta} \\ ie^{-i\theta} & 1 \end{pmatrix}\begin{pmatrix} a_{\rm out} \\ b_{\rm out} \end{pmatrix}. \tag{17}$$

The phase θ can be controlled using a phase shifter and we hereafter set $\theta = -\pi/2$. Then, Eqs. (13)–(15) become

$$\frac{d}{dt}\sigma = -\frac{\Gamma_t}{2}\sigma - f(t)[\sigma^\dagger,\sigma] + \sqrt{2\Gamma}[\sigma^\dagger,\sigma]a'_{\rm in}(t) + i\sqrt{\gamma}[\sigma^\dagger,\sigma]c_{\rm in}(t), \tag{18}$$

$$a'_{\rm out}(t) = -a'_{\rm in}(t) - \sqrt{2\Gamma}\sigma(t), \tag{19}$$

$$b'_{\rm out}(t) = b'_{\rm in}(t). \tag{20}$$

The above equations, together with the initial state vector of Eq. (6), form the basis of our analysis.

B. Photon statistics in the output port

In the present setup, the photons emitted by the dot into the fiber are completely forwarded to the $a'_{\rm out}$ port, as indicated by Eq. (19). We examine the photon statistics of the pulse emitted into this port. We denote the probability that the emitted pulse contains n photons by P_n ($n = 0,1,\dots$). To determine the photon statistics, we first evaluate the the quantity $\langle N_m\rangle$ ($m = 1,2,\dots$) defined by

$$\langle N_m\rangle = \int_0^\infty dt_1 \int_{t_1}^\infty dt_2 \cdots \int_{t_{m-1}}^\infty dt_m \times \langle a'^\dagger_{\rm out}(t_1)\cdots a'^\dagger_{\rm out}(t_m) a'_{\rm out}(t_m)\cdots a'_{\rm out}(t_1)\rangle, \quad (21)$$

where $\langle\cdots\rangle = \langle\psi_i|\cdots|\psi_i\rangle$. Using the fact that $a'_{\rm in}(t)$ commutes with $\sigma(t')$ for $t > t'$ due to the causality and that $\langle a'_{\rm in}(t)\rangle = 0$ because there is no input field from this port, $\langle N_m\rangle$ can be rewritten as

$$\langle N_m\rangle = (2\Gamma)^m \int_0^\infty dt_1 \int_{t_1}^\infty dt_2 \cdots \int_{t_{m-1}}^\infty dt_m \times \langle \sigma^\dagger(t_1)\cdots\sigma^\dagger(t_m)\sigma(t_m)\cdots\sigma(t_1)\rangle. \quad (22)$$

The formula to determine P_n from $\langle N_m\rangle$ is obtained by considering a classical pulse in the output port (see Appendix A). We have

$$P_n = \sum_{m=n}^\infty (-1)^{m-n}\, {}_m\mathrm{C}_n \langle N_m\rangle, \quad (23)$$

where ${}_m\mathrm{C}_n$ stands for the binomial coefficient.

C. Evaluation of $\langle N_m\rangle$

In order to evaluate $\langle N_1\rangle$, we consider $\alpha_1(t) = \langle\sigma(t)\rangle$ and $\beta_1(t) = \langle\sigma^\dagger(t)\sigma(t)\rangle$. The equations of motion are derived from Eqs. (6) and (18). Since $\langle a'_{\rm in}\rangle = \langle c_{\rm in}\rangle = 0$ and α_1 is real with resonant driving, we obtain

$$\frac{d}{dt}\begin{pmatrix}\alpha_1\\ \beta_1\end{pmatrix} = \begin{pmatrix}-\Gamma_t/2 & -2f(t)\\ 2f(t) & -\Gamma_t\end{pmatrix}\begin{pmatrix}\alpha_1\\ \beta_1\end{pmatrix} + \begin{pmatrix}f(t)\\ 0\end{pmatrix}. \quad (24)$$

The initial condition is $\alpha_1(0) = \beta_1(0) = 0$. For a rectangular pulse of Eq. (7), $f(t)$ vanishes for $t > T$. Therefore, $\beta_1(t)$ can be written as

$$\beta_1(t) = \begin{cases} h(t) & (0 < t < T),\\ h(T)e^{\Gamma_t(T-t)} & (T < t),\end{cases} \quad (25)$$

where $h(t)$ represents the population of the excited state at time t under a continuous drive field. From Eq. (24), the Laplace transform of $h(t)$, $\mathcal{L}_h(z) = \int_0^\infty dt e^{-zt}h(t)$, is given by

$$\mathcal{L}_h(z) = \frac{\Omega^2}{2(z-\lambda_1)(z-\lambda_2)(z-\lambda_3)}, \quad (26)$$

where $\lambda_3 = 0$ and $\lambda_{1,2}$ are the two roots of

$$(z+\Gamma_t/2)(z+\Gamma_t) + \Omega^2 = 0. \quad (27)$$

$h(t)$ is determined by the inverse Laplace transform of $\mathcal{L}_h(z)$. $\langle N_1\rangle$ is then given by $\langle N_1\rangle = \int_0^T dt\, h(t) + \frac{h(T)}{\Gamma_t}$.

As proven in Appendix B, higher-order quantities $\langle N_m\rangle$ ($m = 1,2,\dots$) can be calculated similarly. $\langle N_m\rangle$ is obtained using

$$\langle N_m\rangle = \int_0^T dt\, h_m(t) + \frac{h_m(T)}{\Gamma_t}, \quad (28)$$

where $h_m(t)$ can be determined with the inverse Laplace transform of $\mathcal{L}_{h_m}(z) = [\mathcal{L}_h(z)]^m$. $h_m(t)$ is then given by

$$h_m(t) = \sum_{k=1}^m \left[C^{(1)}_{mk}\, t^{k-1}e^{\lambda_1 t} + C^{(2)}_{mk}\, t^{k-1}e^{\lambda_2 t} + C^{(3)}_{mk}\, t^{k-1}e^{\lambda_3 t}\right], \quad (29)$$

$$C^{(1)}_{mk} = \frac{1}{(k-1)!}\frac{(2E^2)^m}{(\lambda_1-\lambda_2)^m(\lambda_1-\lambda_3)^m} \times \sum_{j=0}^{m-k}\left(\prod_{\mu=1}^{j}\frac{-m-\mu+1}{\mu(\lambda_1-\lambda_2)}\prod_{\nu=1}^{m-k-j}\frac{-m-\nu+1}{\nu(\lambda_1-\lambda_3)}\right). \quad (30)$$

$C^{(2)}_{mk}$ and $C^{(3)}_{mk}$ are obtained by cyclic permutation of λ_1, λ_2, and λ_3 in $C^{(1)}_{mk}$.

IV. NUMERICAL RESULTS

In this section, we present the numerical results. Assuming that a semiconductor quantum dot is used as an emitter, we employ the following parameters: $(g,\kappa,\gamma)/2\pi = (200,1000,5)$ MHz.

A. Excited-state population

First we investigate the excited-state population of the dot, $\langle\sigma^\dagger\sigma\rangle$, assuming continuous driving. It is evaluated using the inverse Laplace transform of $\mathcal{L}_h(z)$ from Eq. (26). The temporal evolution is determined by the two roots of Eq. (27). For a weak drive satisfying $\Omega < \Gamma_t/4$ (the overdamping regime), where Γ_t is the decay rate of the dot, the excited-state population increases monotonically. In contrast, for a strong drive satisfying $\Omega > \Gamma_t/4$ (the damped-oscillation regime), the excited-state population exhibits damped Rabi oscillations [29]. The stationary value is given for both regimes

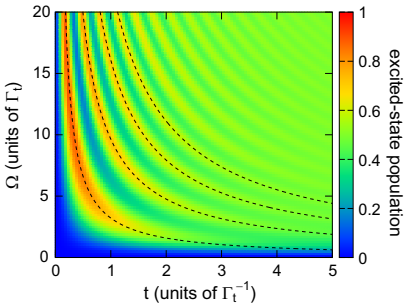

FIG. 2. (Color online) Excited-state population as a function of time t and Rabi frequency Ω. Thin dotted lines indicate $\Omega t = \pi$, 3π, 5π, and 7π (left to right). The Rabi oscillations are damped for $t \gtrsim \Gamma_t^{-1}$.

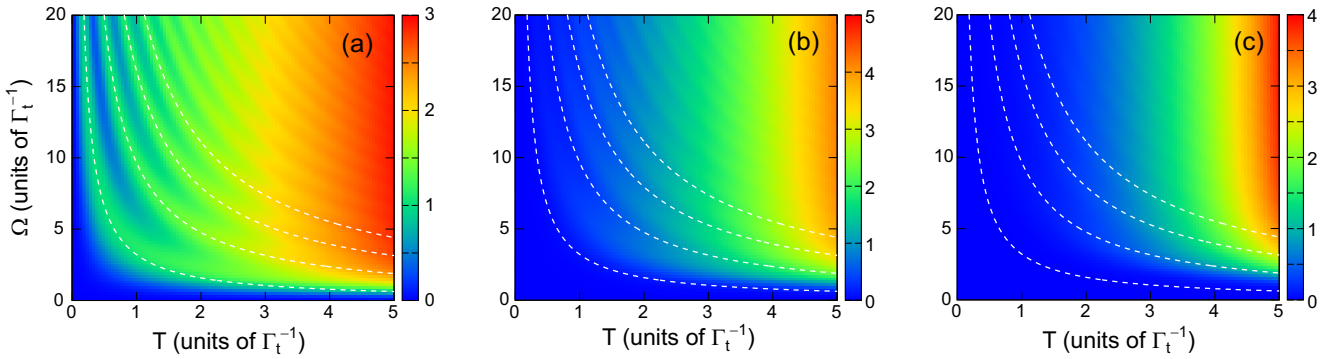

FIG. 3. (Color online) (a) $\langle N_1 \rangle$, (b) $\langle N_2 \rangle$, and (c) $\langle N_3 \rangle$ as functions of the pulse length T and the Rabi frequency Ω. White dashed lines indicate $\Omega T = \pi, 3\pi, 5\pi$, and 7π (left to right).

by

$$\langle \sigma^\dagger \sigma \rangle_s = \frac{\Omega^2}{2\Omega^2 + \Gamma_t^2}. \tag{31}$$

In Fig. 2, the excited-state population is plotted as a function of the drive amplitude Ω and the time t. For a short time ($t \lesssim \Gamma_t^{-1}$), the excited-state population is determined solely by the pulse area, Ωt. It is maximized (minimized) when $\Omega t \simeq (2n+1)\pi$ ($2n\pi$), exhibiting Rabi oscillations. For a long time ($t \gtrsim \Gamma_t^{-1}$), the oscillatory behavior is damped and approaches the stationary value determined by Eq. (31).

B. $\langle N_m \rangle$ and P_n

In this section, we discuss the results for pulsed excitation. In Fig. 3, $\langle N_m \rangle$ ($m = 1,2,3$) is plotted as functions of the pulse length T and amplitude Ω. $\langle N_1 \rangle$ represents the mean photon number contained in the pulse emitted by the dot. Figure 3(a) shows that $\langle N_1 \rangle$ exhibits oscillatory behavior in the short-pulse region ($T \lesssim \Gamma_t^{-1}$): $\langle N_1 \rangle \simeq 1$ for $\Omega T \simeq (2n+1)\pi$ and $\langle N_1 \rangle \simeq 0$ for $\Omega T \simeq 2n\pi$. This is because the dot excitation is almost completely emitted into the target fiber mode and is a natural result of the Rabi oscillation of the dot. Accordingly, Figs. 2(b) and 3(a) almost coincide for $T \lesssim \Gamma_t^{-1}$. In the long-pulse region ($T \gtrsim \Gamma_t^{-1}$), emission and reexcitation occur repeatedly in the dot, and accordingly $\langle N_1 \rangle$ increases monotonically as the pulse gets longer. For $\langle N_2 \rangle$ ($\langle N_3 \rangle$), which take nonzero values when the emitted pulse contains more than two (three) photons, clear oscillatory behavior is unobservable. $\langle N_2 \rangle$ and $\langle N_3 \rangle$ increase monotonically for longer and stronger pulses.

Next, we discuss the photon statistics of the output pulse. As discussed in Appendix A, the n-photon probabilities P_n ($n = 0,1,\ldots$) are determined from $\langle N_m \rangle$ ($m = 1,2,\ldots$). In principle, infinite values of $\langle N_m \rangle$ ($1 \leqslant m \leqslant \infty$) are required to determine P_n. However, reliable numerical results can be obtained by restricting m to $1 \leqslant m \leqslant 8$ in the following numerical results. Figure 4 plots P_0, P_1, and P_2 as functions of the pulse length T and amplitude Ω. In the short-pulse region ($T \lesssim \Gamma_t^{-1}$), where the dot exhibits coherent Rabi oscillations, P_0 and P_1 exhibit contrastive behavior: $P_0 \simeq 0$ and $P_1 \simeq 1$ for $\Omega T \simeq (2n+1)\pi$, whereas $P_0 \simeq 1$ and $P_1 \simeq 0$ for $\Omega T \simeq 2n\pi$. P_2 almost vanishes in this region, indicating the absence of emission and reexcitation within the duration of the short pulse. Thus, the output pulse functions as an ideal single photon ($P_1 \simeq 1$ and the others vanish) by setting $\Omega T = (2n+1)\pi$. In the long-pulse region ($T \gtrsim \Gamma_t^{-1}$), the zero-photon probability P_0 decreases whereas the multiphoton probability P_2 increases in general. This is because the possibility of emission and reexcitation of the dot increases for long pulses. In contrast with the multiphoton components of $\langle N_m \rangle$ [Figs. 3(b) and 3(c)], clear oscillatory behavior is observable even for the multiphoton probability: P_2 is maximized (minimized) for $\Omega T \simeq 2n\pi$ [$(2n+1)\pi$], reflecting the oscillatory behavior of P_1.

In Fig. 5 the dependences of P_n ($n = 0,\ldots,3$) on the pulse length T are shown, fixing the pulse area ΩT at π, 2π, and 3π. It is observed that similar photon statistics result for π

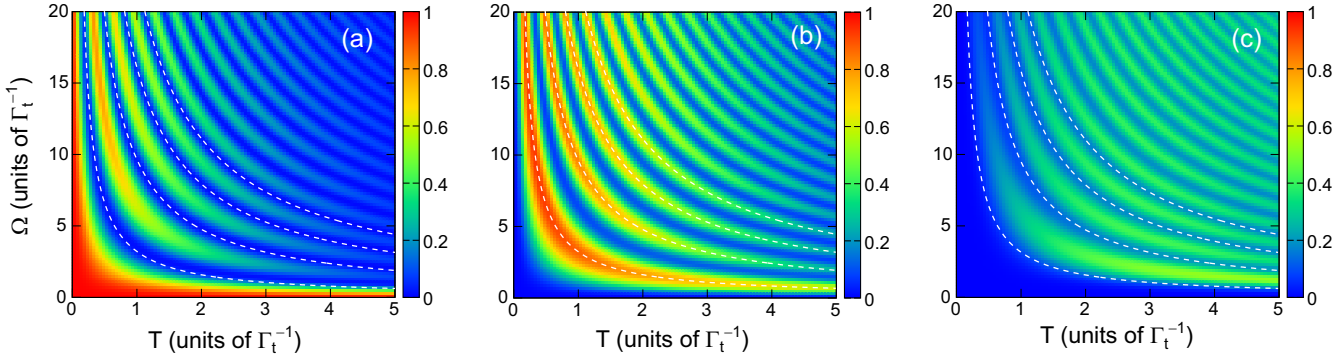

FIG. 4. (Color online) (a) P_0, (b) P_1, and (c) P_2 as functions of the pulse length T and the Rabi frequency Ω. White dashed lines indicate $\Omega T = \pi, 3\pi, 5\pi$, and 7π (left to right).

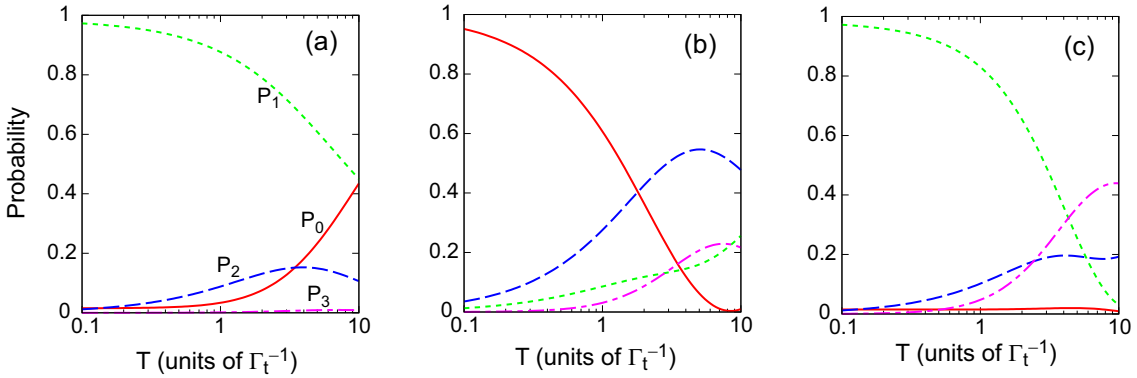

FIG. 5. (Color online) Plots of P_0 (red solid line), P_1 (green dotted line), P_2 (blue dashed line), and P_3 (magenta dashed-dotted line) fixing the pulse area ΩT at (a) $\Omega T = \pi$, (b) $\Omega T = 2\pi$, and (c) $\Omega T = 3\pi$.

and 3π pulses [Figs. 5(a) and 5(c)]. In light of single-photon generation, shorter drive pulses are advantageous. The ideal single-photon state ($P_1 \simeq 1$ and the others vanish) is realized for $T \lesssim \Gamma_t^{-1}$. P_1 is gradually lost for longer drive pulses. Instead, P_0 becomes dominant in the case of the π pulse, whereas the multiphoton probabilities become dominant in the case of the 3π pulse. For a 2π pulse [Fig. 5(b)], P_0 is dominant for small T and P_2 is dominant for large T. Interestingly, P_2 is always larger than P_1 and exceeds 0.5 with a proper drive pulse length. Therefore, the 2π-pulse excitation using a relatively long drive pulse is applicable to the generation of two-photon pulses.

In Fig. 6, $g^{(2)}(0) = (\langle n^2\rangle - \langle n\rangle)/\langle n\rangle^2$ is plotted as a function of the pulse length T, where $\langle n\rangle = \sum_{n=0}^{\infty} n P_n$ (mean photon number in the pulse) and $\langle n^2\rangle = \sum_{n=0}^{\infty} n^2 P_n$. $g^{(2)} < 1$ indicates the sub-Poissonian photon statistics and therefore the nonclassicalness of the generated pulse. When the pulse length is short ($T \lesssim \Gamma_t^{-1}$), we observe contrastive dependence of the photon statistics on the pulse area: The photon statistics is sub-Poissonian (super-Poissonian) when the pulse area is odd (even) multiples of π. In contrast, as the pulse length becomes longer ($T \gtrsim \Gamma_t^{-1}$), the photon statistics gradually approaches the Poissonian regardless of the pulse area.

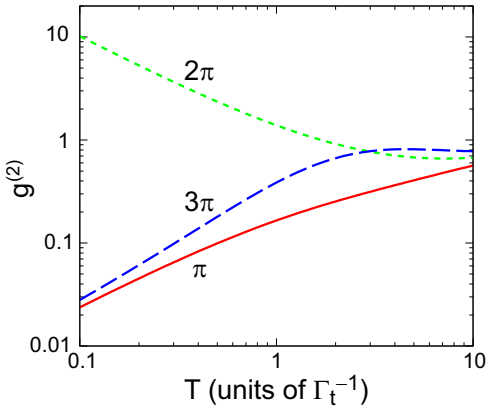

FIG. 6. (Color online) Plots of $g^{(2)}(0)$ as a function of the pulse length T. The pulse area ΩT is fixed at π (red solid line), 2π (green dotted line), and 3π (blue dashed line).

V. SUMMARY

In this article, we theoretically investigated resonance fluorescence from a single emitter after pulsed excitation. We considered a microtoroidal cavity QED system in the weak-coupling regime, where radiation from the emitter is guided nearly perfectly into a target fiber mode. We derived analytic formulas to rigorously evaluate the photon statistics of the output pulse. By applying a π or 3π pulse to the emitter whose pulse length is shorter than the lifetime of the emitter, we can deterministically generate a nearly ideal single photon propagating in a fiber. In contrast, by applying a 2π pulse whose pulse length is comparable to the lifetime, we can generate a photon pulse in which the two-photon component is dominant. The current results are useful for the estimation of the photon statistics of practical single-photon sources.

ACKNOWLEDGMENT

This research was partially supported by SCOPE (111507004), MEXT KAKENHI (25400417), NICT Commissioned Research, and the Research Foundation for Opto-Science and Technology.

APPENDIX A: RELATION BETWEEN $\langle N_m\rangle$ AND P_n

First, we derive a formula to express $\langle N_m\rangle$ in terms of P_n. Throughout this Appendix, we denote $a'_{\rm out}(t)$ by a_t for simplicity. We define the photon number operator in the output port by $\hat{n} = \int_0^\infty dt\ a_t^\dagger a_t$. Then $\hat{N}_1 = \hat{n}$. $\hat{N}_2$ can be written as $\hat{N}_2 = \int_0^\infty dt \int_0^\infty dt' a_t^\dagger a_{t'}^\dagger a_{t'} a_t/2 = \int_0^\infty dt\ a_t^\dagger \hat{n} a_t/2$. Using $[\hat{n}, a_t] = -a_t$, $\hat{N}_2$ can be rewritten as $\hat{N}_2 = \hat{n}(\hat{n}-1)/2$. Similarly, we have $\hat{N}_m = \hat{n}\cdots(\hat{n}-m+1)/m!$. Therefore,

$$\langle N_m\rangle = \sum_{n=m}^{\infty} {}_n\mathrm{C}_m P_n, \tag{A1}$$

where ${}_n\mathrm{C}_m$ stands for the binomial coefficient.

Next, we derive a formula to express P_n in terms of $\langle N_m\rangle$. For this purpose, we consider a classical pulse $|\alpha\rangle$. Since it is an eigenstate of the field annihilation operator,

we immediately have $\langle N_m \rangle = |\alpha|^{2m}/m!$. On the other hand, the photon statistics of a classical pulse obey the Poissonian, $P_n = e^{-|\alpha|^2}|\alpha|^{2n}/n!$. Expanding the exponential, it becomes $P_n = \sum_{m=n}^{\infty}(-1)^{m-n}{}_m\mathrm{C}_n \frac{m!}{n!(m-n)!}|\alpha|^{2m}m!$. Therefore,

$$P_n = \sum_{m=n}^{\infty}(-1)^{m-n}{}_m\mathrm{C}_n\langle N_m\rangle. \tag{A2}$$

We note that a more general derivation of this formula is presented in Ref. [29].

APPENDIX B: EVALUATION OF $\langle N_2 \rangle$

Here, we discuss the method to evaluate $\langle N_2\rangle$. For this purpose, we investigate $\alpha_2(t_1,t_2) = \langle\sigma^\dagger(t_1)\sigma(t_2)\sigma(t_1)\rangle$ and $\beta_2(t_1,t_2) = \langle\sigma^\dagger(t_1)\sigma^\dagger(t_2)\sigma(t_2)\sigma(t_1)\rangle$, where $t_1 < t_2$. Since $\sigma(t_1)$ commutes with $a'_{\mathrm{in}}(t_2)$ and $c_{\mathrm{in}}(t_2)$, we obtain

$$\frac{d}{dt_2}\begin{pmatrix}\alpha_2\\ \beta_2\end{pmatrix} = \begin{pmatrix}-\Gamma_t/2 & -2f(t_2)\\ 2f(t_2) & -\Gamma_t\end{pmatrix}\begin{pmatrix}\alpha_2\\ \beta_2\end{pmatrix} + \begin{pmatrix}\beta_1(t_1)f(t_2)\\ 0\end{pmatrix}. \tag{B1}$$

The initial condition is $\alpha_2(t_1,t_1) = \beta_2(t_1,t_1) = 0$. Comparing Eqs. (24) and (B1), $\beta_2(t_1,t_2)$ is given by

$$\beta_2(t_1,t_2) = \begin{cases} h(t_1)h(t_2-t_1) & (t_1 < t_2 < T),\\ h(t_1)h(T-t_1)e^{\Gamma_t(T-t_2)} & (t_1 < T < t_2),\\ 0 & (T < t_1 < t_2).\end{cases} \tag{B2}$$

Then, $\langle N_2\rangle$ is given by

$$\langle N_2\rangle = \int_0^T dt h_2(t) + \frac{h_2(T)}{\Gamma_t}, \tag{B3}$$

where $h_2(t) = \int_0^t dt_1 h(t_1)h(t-t_1)$. Since h_2 is a convolution of h, its Laplace transform is given by $\mathcal{L}_{h_2}(z) = [\mathcal{L}_h(z)]^2$.

[1] H. J. Kimble, M. Dagenais, and L. Mandel, Phys. Rev. Lett. **39**, 691 (1977).
[2] R. Short and L. Mandel, Phys. Rev. Lett. **51**, 384 (1983).
[3] J. McKeever, A. Boca, A. D. Boozer, R. Miller, J. R. Buck, A. Kuzmich, and H. J. Kimble, Science **303**, 1992 (2004).
[4] B. Darquié, M. P. A. Jones, J. Dingjan, J. Beugnon, S. Bergamini, Y. Sortais, G. Messin, A. Browaeys, and P. Grangier, Science **309**, 454 (2005).
[5] J. D. Thompson, T. G. Tiecke, N. P. de Leon, J. Feist, A. V. Akimov, M. Gullans, A. S. Zibrov, V. Vuletić, and M. D. Lukin, Science **340**, 1202 (2013).
[6] C.-L. Hung, S. M. Meenehan, D. E. Chang, O. Painter, and H. J. Kimble, New J. Phys. **15**, 083026 (2013).
[7] F. Diedrich and H. Walther, Phys. Rev. Lett. **58**, 203 (1987).
[8] M. Keller, B. Lange, K. Hayasaka, W. Lange, and H. Walther, Nature (London) **431**, 1075 (2004).
[9] C. Kurtsiefer, S. Mayer, P. Zarda, and H. Weinfurter, Phys. Rev. Lett. **85**, 290 (2000).
[10] R. Brouri, A. Beveratos, J.-P. Poizat, and P. Grangier, Opt. Lett. **25**, 1294 (2000).
[11] A. Beveratos, R. Brouri, T. Gacoin, J.-P. Poizat, and P. Grangier, Phys. Rev. A **64**, 061802(R) (2001).
[12] A. Beveratos, R. Brouri, T. Gacoin, A. Villing, J.-P. Poizat, and P. Grangier, Phys. Rev. Lett. **89**, 187901 (2002).
[13] P. Michler, A. Imamoğlu, M. D. Mason, P. J. Carson, G. F. Strouse, and S. K. Buratto, Nature (London) **406**, 968 (2000).
[14] P. Michler, A. Kiraz, C. Becher, W. V. Schoenfeld, P. M. Petroff, L. Zhang, E. Hu, and A. Imamoğlu, Science **290**, 2282 (2000).
[15] C. Santori, M. Pelton, G. Solomon, Y. Dale, and Y. Yamamoto, Phys. Rev. Lett. **86**, 1502 (2001).
[16] V. V. Klimov and M. Ducloy, Phys. Rev. A **69**, 013812 (2004).
[17] F. Le Kien, S. Dutta Gupta, V. I. Balykin, and K. Hakuta, Phys. Rev. A **72**, 032509 (2005).
[18] K. P. Nayak, P. N. Melentiev, M. Morinaga, F. L. Kien, V. I. Balykin, and K. Hakuta, Opt. Express **15**, 5431 (2007).
[19] E. Vetsch, D. Reitz, G. Sagué, R. Schmidt, S. T. Dawkins, and A. Rauschenbeutel, Phys. Rev. Lett. **104**, 203603 (2010).
[20] M. Das, A. Shirasaki, K. P. Nayak, M. Morinaga, F. L. Kien, and K. Hakuta, Opt. Express **18**, 17154 (2010).
[21] A. Goban, K. S. Choi, D. J. Alton, D. Ding, C. Lacroûte, M. Pototschnig, T. Thiele, N. P. Stern, and H. J. Kimble, Phys. Rev. Lett. **109**, 033603 (2012).
[22] M. Fujiwara, K. Toubaru, T. Noda, H.-Q. Zhao, and S. Takeuchi, Nano Lett. **11**, 4362 (2011).
[23] T. Schröder, M. Fujiwara, T. Noda, H.-Q. Zhao, O. Benson, and S. Takeuchi, Opt. Express **20**, 10490 (2012).
[24] R. Yalla, F. Le Kien, M. Morinaga, and K. Hakuta, Phys. Rev. Lett. **109**, 063602 (2012).
[25] T. Aoki, B. Dayan, E. Wilcut, W. P. Bowen, A. S. Parkins, T. J. Kippenberg, K. J. Vahala, and H. J. Kimble, Nature (London) **443**, 671 (2006).
[26] B. Dayan, A. S. Parkins, D. J. Alton, C. A. Regal, B. Dayan, E. Ostby, K. J. Vahala, and H. J. Kimble, Science **319**, 1062 (2008).
[27] T. Aoki, A. S. Parkins, D. J. Alton, C. A. Regal, B. Dayan, E. Ostby, K. J. Vahala, and H. J. Kimble, Phys. Rev. Lett. **102**, 083601 (2009).
[28] D. J. Alton, N. P. Stern, T. Aoki, H. Lee, E. Ostby, K. J. Vahala, and H. J. Kimble, Nat. Phys. **7**, 159 (2011).
[29] W. Vogel and D.-G. Welsch, *Quantum Optics* (Wiley-VCH, New York, 2006).